RSC Advances

ROYAL SOCIETY OF CHEMISTRY

PAPER

View Article Online
View Journal | View Issue

Cite this: *RSC Adv.*, 2021, **11**, 7521

Atomic layer deposition of superparamagnetic ruthenium-doped iron oxide thin film

Aile Tamm, *[a] Aivar Tarre,[a] Jekaterina Kozlova,[a] Mihkel Rähn,[a] Taivo Jõgiaas,[a] Tauno Kahro,[a] Joosep Link[b] and Raivo Stern[b]

Received 20th January 2021
Accepted 7th February 2021

DOI: 10.1039/d1ra00507c

rsc.li/rsc-advances

Due to the several applications of biosensors, such as magnetic hyperthermia and magnetic resonance imaging, the use of superparamagnetic nanoparticles or thin films for preparing biosensors has increased greatly. We report herein on a strategy to fabricate a nanostructure composed of superparamagnetic thin films. Ruthenium-doped iron oxide thin films were deposited by using atomic layer deposition at 270 and 360 °C. $FeCl_3$ and $Ru(EtCp)_2$ were used as metal precursors and H_2O/O_2 as the oxygen precursor. Doping with ruthenium helps to lower the formation temperature of hematite (α-Fe_2O_3). Ruthenium content was changed from 0.42 at% up to 29.7 at%. Ru-doped films had a nano-crystallized structure of hematite with nanocrystal sizes from 4.4 up to 7.8 nm. Magnetization at room temperature was studied in iron oxide and Ru-doped iron oxide films. A new finding is a demonstration that in a Ru-doped iron oxide thin film superparamagnetic behavior of nanocrystalline materials (α-Fe_2O_3) is observed with the maximum magnetic coercive force H_c of 3 kOe. Increasing Ru content increased crystallite size of hematite and resulted in a lower blocking temperature.

Introduction

The most basic principle of magnetism, *i.e.* magnetic interaction at a distance, empowers the development of applications of biosensors, such as cancer and gene therapy, developmental biology or as protection layers of materials against viruses, SARS-CoV-2, *etc.* A popular example, superparamagnetic nanoparticles will be more and more used in a wide range of biomedical applications, such as magnetic hyperthermia and other magnetism-based health applications.[1–3] However, several effective magnetic particles present a danger to living organisms because nanoparticles may have direct toxic properties and also due to other factors, such as particle aggregation.[4,5] These circumstances can have catastrophic consequences, as clustered particles may block blood flow if applied *in vivo*.

However, by inducing nanoparticles inside a thin film substance it is possible to increase the safety and stability of magnetic nanoparticles. By using atomic layer deposition (ALD) it will be possible to achieve conformal deposition with atomic precision on various nanostructured architectures, for example, different sizes of nanocrystals (nanoparticles) with large or complicated surfaces.[6] ALD is a chemical vapor phase technique capable of producing thin films, which are based on sequential, self-limiting reactions. ALD offers an exceptional conformality on high aspect ratio structures, also the thickness control on the atomic level.[7]

Iron oxide in the hematite phase (α-Fe_2O_3) in the form of small nanoparticles with superparamagnetic behavior can be said to be one of the most studied nanomaterial.[1,3,4,8,9] Also, the iron oxide in the form of ALD thin film is quite well known,[7] but nanocrystalline hematite thin film showing superparamagnetic behavior and, deposited at lower temperatures, has not yet been shown.

In the present study, the target material of nanocrystalline hematite thin films was achieved at a quite low temperature of 270 °C (instead of typical 360 °C).[10] For achieving such a low-temperature crystallization the doping with ruthenium was used. Thickness, nanostructure, morphology, and magnetic behavior of the deposited thin films and, complementarily, cross-sections of the selected films deposited on three-dimensional (3D) substrates were examined.

Morphology and structure

On a planar Si(100) substrate, the mean growth rate of the iron oxide films grown at 270 up to 360 °C in $FeCl_3 + H_2O$ process was ~0.09 ± 0.01 nm per cycle. The growth rate of iron oxide in the $FeCl_3 + H_2O/O_2$ process was slightly higher, 0.10 ± 0.02 nm per cycle, most probably because the oxygen activates the oxidation process of iron precursor. The growth rates of iron oxide were calculated from X-ray fluoresence (XRF) measurements, only Fe mass thicknesses were presented in Fig. 1. The second oxidizer O_2 was included to the process for dopant metal precursor $Ru(EtCp)_2$.[11] At 270 °C, the mean growth rate was as low as

[a]*Institute of Physics, University of Tartu, W. Ostwaldi Str. 1, 50411 Tartu, Estonia. E-mail: aile.tamm@ut.ee; Tel: +372 737 4662*

[b]*National Institute of Chemical Physics and Biophysics, Akadeemia tee 23, 12618 Tallinn, Estonia*

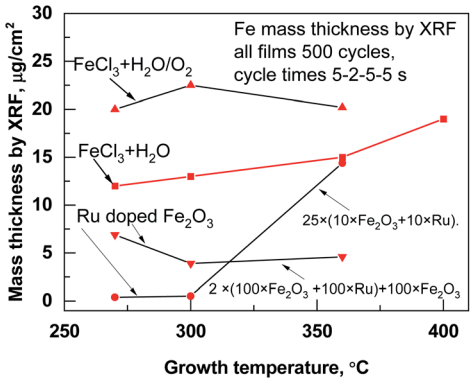

Fig. 1 Mass thicknesses measured by XRF inside the films deposited at different temperatures and processes.

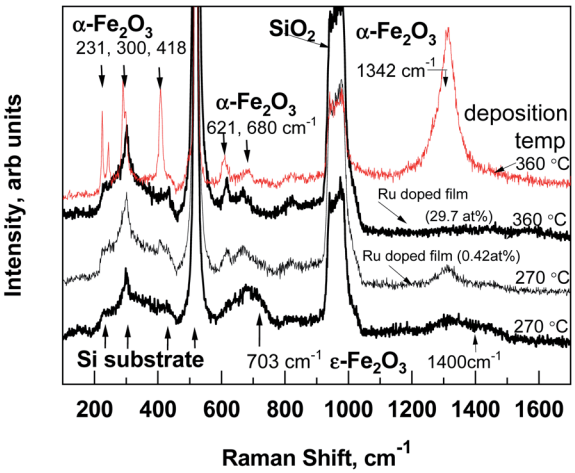

Fig. 2 Room-temperature micro-Raman spectra of pure iron oxide and Ru-doped structures, the recognized Raman bands are denoted by labels.

0.022 nm per cycle for 500 cycles Ru films on the Si substrate made with cycle times 5–2–5–5 s, being similar to the growth rate observed previously by Kukli *et al.*,[10] but at $T = 360$ °C, the growth rate was somewhat increased up to 0.03 nm per cycles. Thicknesses and composition of thin films deposited at different temperatures are presented in Table 1. When increasing the amount of ruthenium into iron oxide, the growth rate was changed and one could see that the estimated actual growth rates for iron oxide layers tended to decrease with the number of the Ru deposition cycles.

This could be expected, considering that, at the beginning of the ALD growth, the dependence of the film thickness on the number of cycles most often remains sublinear and the growth rate somewhat retards, due to the nucleation issues at the early stages of the growth.

Regarding the results of micro-Raman spectroscopy (Fig. 2) at 270 °C deposited iron oxide, the main bands at 703 and 1400 cm^{-1}, which are typical for ε-Fe_2O_3, were observed.[12] At 360 °C deposited iron oxide thin film the broad bands at 231, 300, 418, 621, 680 and 1342 cm^{-1} were observed, which are typical for α-Fe_2O_3.[13] At 270 °C deposited Ru-doped iron oxide thin films, the main broad bands of hematite (α-Fe_2O_3) at 418, 621, 680 and 1320 cm^{-1} could be noticed. Since the films are very thin, some of the bands are hidden under the reflexes caused by the Si substrate (200–521 cm^{-1}).

GIXRD patterns (Fig. 3) confirmed that all thin iron oxide films were crystallized already in the as-deposited state at both deposition temperatures. The diffractogram of the pure iron oxide thin film (Fig. 3, top panel) contained reflections attributable to the hematite α-Fe_2O_3 (PDF 00-033-0664), deposited at 360 °C and orthorhombic ε-Fe_2O_3 phase (ICSD 173024), deposited at 270 °C. This metastable ε-Fe_2O_3 phase has been found and synthesized only in nanoscale samples, including specimens in a thin film form.[10,14] In an ALD study the ε-Fe_2O_3 phase was present in a lower deposition temperature range (280–320 °C),[10] and at temperatures higher than 340 °C the phase had changed to hematite.[14] In a pure Ru film the hexagonal Ru phase (PDF 00-006-0663) was detected and the GIXRD peaks at 38.4, 42.1, 44.0, 58.3 and 69.4 degrees were observed. Ru-doped iron oxide thin films have very broad reflections of a hematite phase (Fig. 3, bottom panel), the main GIXRD

Table 1 Film recipes, thicknesses (by XRR), growth rates, Ru and Cl mass thicknesses (by XRF) of single oxides, and Ru-doped structures

Name of the sample with deposition temperature	ALD growth cycle sequence	Thickness nm	Ru, µg cm^{-2}	Cl, µg cm^{-2}
Iron oxide, at 270 °C	500 × ($FeCl_3$ – H_2O/O_2)	49.9	—	0.06
Ruthenium at 270 °C	500 × (Ru(Et(Cp)$_2$) – H_2O/O_2)	15.8	17.4	—
Ru-doped Fe_2O_3 at 270 °C, at% (Ru) = 0.42	2 × (100 × ($FeCl_3$ – H_2O/O_2) + 100 × (Ru(Et(Cp)$_2$) – H_2O/O_2)) + 100 × ($FeCl_3$ – H_2O/O_2)	24.1	0.2	0.12
Ru-doped Fe_2O_3 at 270 °C, at% (Ru) = 0.98	25 × (10 × $FeCl_3$ – H_2O/O_2 + 10 × Ru(Et(Cp)$_2$) – H_2O/O_2)	28.0	0.4	0.22
Ruthenium at 360 °C	500 × (Ru(Et(Cp)$_2$) – H_2O/O_2)	20.1	22.5	—
Ru-doped Fe_2O_3 at 360 °C, at% (Ru) = 29.77	25 × (10 × $FeCl_3$ – H_2O/O_2 + 10 × Ru(Et(Cp)$_2$) – H_2O/O_2)	36.5	14.3	0.03
Iron oxide at 360 °C	500 × ($FeCl_3$ – H_2O/O_2)	52.8	—	0.05

reflection at 33.2 and 54.2 degrees were used for evaluating the size of nano-crystallites in accordance with Scherrer's formula and by using a standard reference material SRM-660 (LaB_6) (the instrumental broadening has to be considered, where the standard deviation is ~1 nm). As expected from the diffractograms presented in Fig. 3, in the case of Ru-doped iron oxide, the estimated size of α-Fe_2O_3 crystallites was 4.4 ± 0.3 nm in Ru-doped film (Ru 0.42 at%) and 7.8 ± 0.4 nm in Ru-doped (Ru 0.98 at%) film.

Fig. 4 shows cross-sectional STEM images of the Ru-doped iron oxide film deposited at 270 °C. Fig. 4 (left panel) displays the cross-sectional view of the bright field (BF) image of the film, showing the areas with distinct lattice planes, which correspond to the domains of different crystalline orientation. This confirms that the crystallization of the iron oxide took place. The film is estimated to be 24.5–27 nm thick, which is in accordance with XRR measurements (Table 1). The thickness variation is due to the roughness of the surface of the film. The crystalline domains in the film vary in size, some of the larger crystallites penetrate the whole thickness of the film, while, smaller crystallites were more abundant. The high-resolution HAADF image (Fig. 4, right panel) shows the presence of crystallites with the size of 4 nm and smaller inside the film. At some places, no crystal fringes can be observed, indicating that some of the amorphous areas were also present in the film.

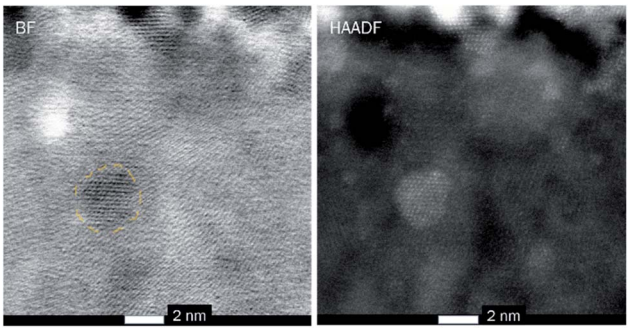

Fig. 4 Cross-sectional STEM images of the sample (2 × (100 × Fe_2O_3 + 100 × Ru) + 100 × Fe_2O_3) structure overview bright field (BF) (left panel) and the edges of one nanocrystal are illustrated. High-angle annular dark field (HAADF) image of the same structure (right panel).

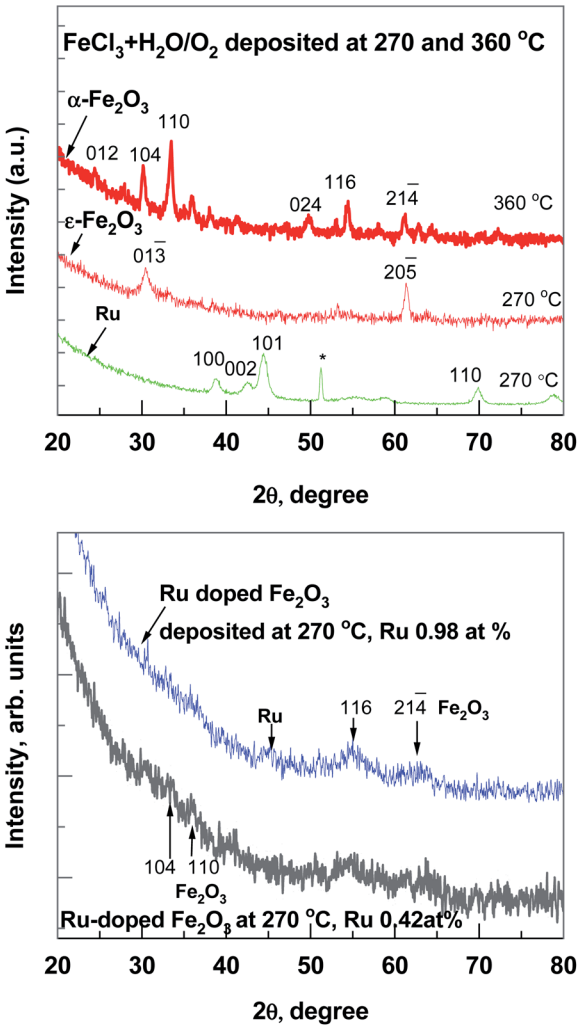

Fig. 3 GIXRD patterns from the Fe_2O_3 and Ru thin films (500 cycles), top panel and Ru-doped iron oxide thin films, bottom panel. Miller indexes, assigned after crystallization, are indicated and * marked reflection comes from substrate.

SEM images of pure Fe_2O_3 and pure Ru thin films, deposited at 270 °C, are shown in Fig. 5. It can be seen, that Fe_2O_3 thin film (Fig. 5a) shows well-defined grains with rounded edges, which uniformly cover the surface. The pure Ru film (Fig. 5b) also shows the grain-like morphology, but the grains have a more faceted shape, and they are smaller in size.

The SEM images of iron oxide films after incorporation of the ruthenium during the deposition process are presented in Fig. 6. It can be seen that the use of ruthenium has led to the decrease in the size of the grains, however, in the case of a Ru-doped structure, the distinct wedge-shaped grains can still be well discerned in the image. The morphology of the higher Ru-doped film has changed more dramatically, showing a very fine-grain structure. The fine grains visible on the surface are probably a structure of the top ruthenium layer deposited during the last 10 cycles. It can be seen, that the surface under the fine-grained top layer is not completely uniform, as would be expected if only isotropic nano-sized grains would be present. This indicates that at least at some places larger grains were also formed inside the iron oxide film.[15]

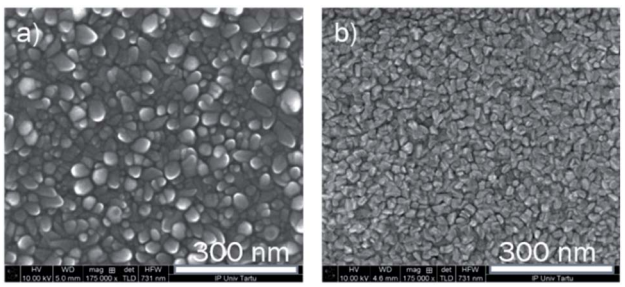

Fig. 5 The bird-eye view of the SEM images of the reference objects Fe_2O_3, (a) and Ru (b) films, both films are deposited at 270 °C.

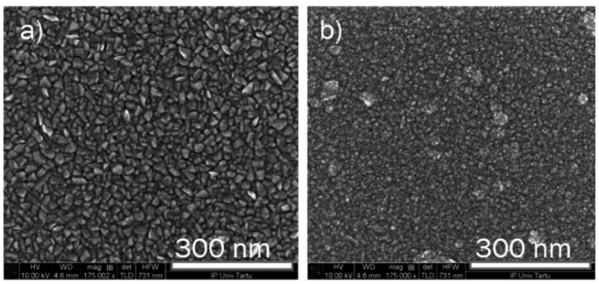

Fig. 6 The bird-eye view of the SEM images of the Ru-doped iron oxide films (0.42 at%, a) and (0.98 at%, b). Both films are deposited at 270 °C.

The conformality of ALD-deposited films is often the critical factor in choosing ALD over the competing deposition techniques. The conformality of high aspect ratio and three-dimensionally-structured (3D) materials is achieved by its self-limiting characteristic, which restricts the reaction at the surface to no more than one layer of precursor. With sufficient precursor pulse times, the precursor can disperse even into deep trenches, allowing for complete reaction with the entire surface (Fig. 7). For example, a good conformality of Ru-doped iron oxide films (deposited at 270 °C with the same cycle times 5–2–5–5 s) was achieved and is shown in Fig. 7c. The thickness of the layer did not decrease noticeably towards the bottom of the trench, though, indicating that the step coverage could not reach 100% (the 3D trench along with its ~1.6 μm depth). The top view of the 3D sample shows that the pore openings were not closed in process of the deposition (Fig. 7a and b).

Magnetic behavior

In-plane magnetic measurements were performed for the pure iron oxide and Ru-doped thin film samples. The hysteresis curves for the films, measured at room temperature, displayed nonlinear magnetization with saturation and well-defined coercive fields in most samples, demonstrating typical ferro- or ferrimagnetic behavior (Fig. 8). α-Fe_2O_3 exhibits a coercive field of 2.8 kOe at room temperature, that increases to 5.5 kOe at low temperature (5 K) (Fig. 8a). For comparison highest coercivity value in case of α-Fe_2O_3 nanomaterials reported so far is 6.2 kOe measured at 300 K and 6 kOe at 4 K.[16] ε-Fe_2O_3 demonstrates a more complex hysteresis (Fig. 8b), that can be deconvoluted into different contributions of different phases following the method proposed by L. Corbellini *et al.*[17] Linear contribution, major and minor hysteresis loop can be extracted. Minor loop with zero coercivity could be assigned to the smallest crystallites with superparamagnetic behavior. Major loop exhibits a huge coercive field of 18 kOe, which is expected in the case of ε-Fe_2O_3.[18]

At the same time, the Ru-doped hematite film show a curve typical of a superparamagnetic material (Fig. 9), but the Ru-doped iron oxide thin film, deposited at 360 °C, has a paramagnetic nature of the material (not shown). Although the Ru-doped films deposited at 270 °C demonstrated a behavior characteristic of a superparamagnetic material (Fig. 9a), the

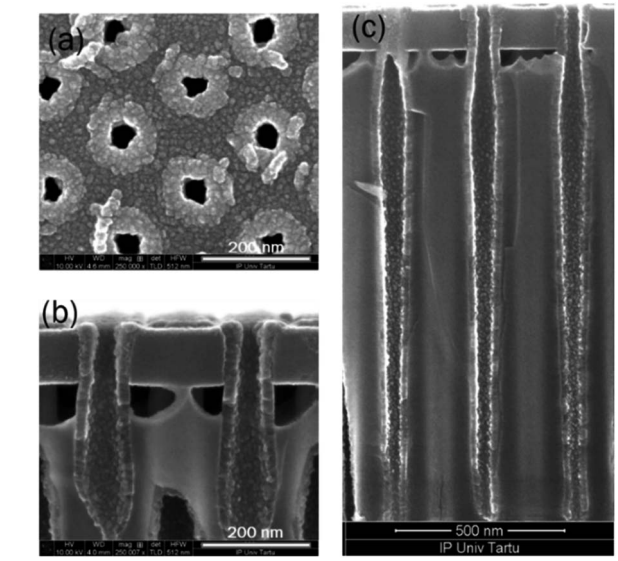

Fig. 7 SEM images of the 3D substrate, top view (a) and cross-section (b and c) of the Ru-doped iron oxide thin film (with recipe 25 × (10 × Fe_2O_3 + 10 × Ru)) on 3D stack substrate.

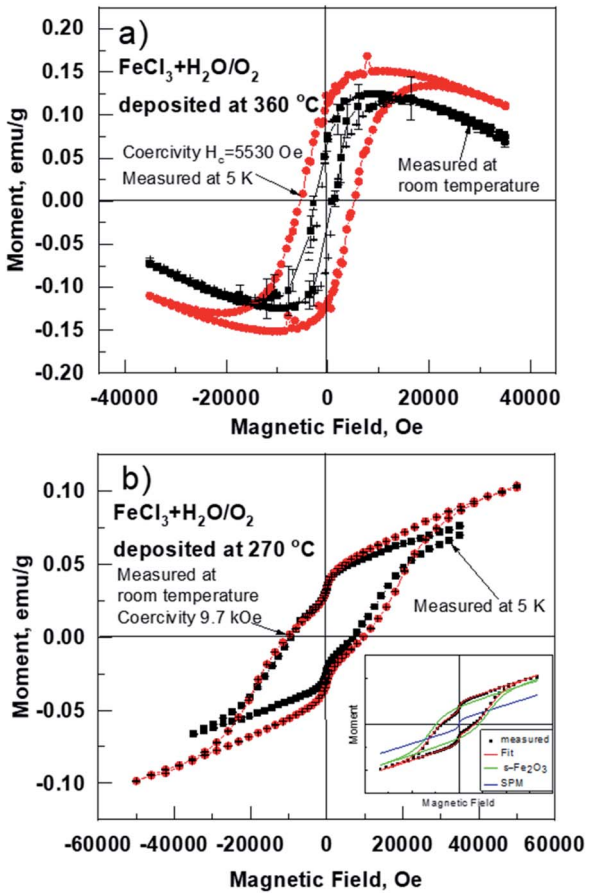

Fig. 8 Magnetization *vs.* external magnetic field curves at room (300 K) and at low temperature (5 K) for the selected as-deposited samples deposited at 360 (a) and 270 °C (b). Substrate diamagnetism has not been subtracted from the data. Deconvolution of different contributions to the hysteresis loops are depicted in the inset of (b).

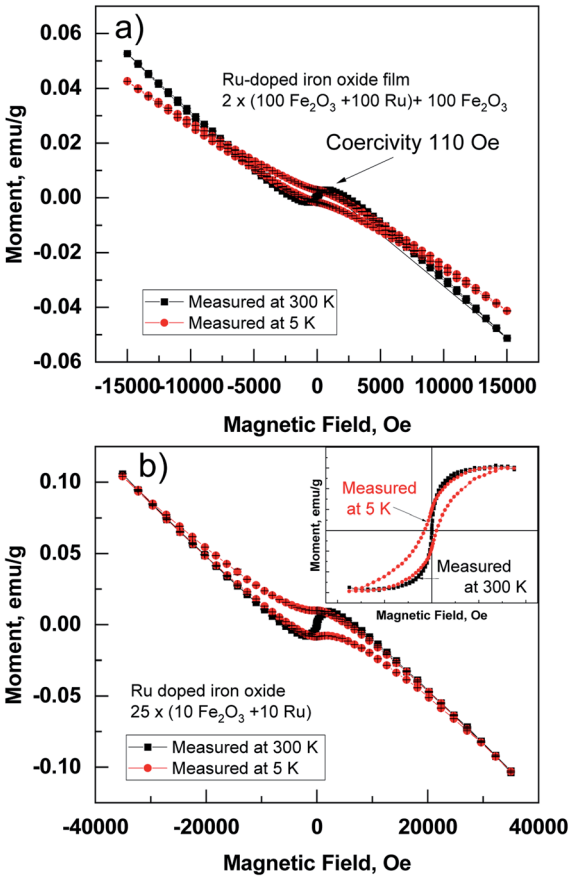

Fig. 9 Magnetic moment *versus* magnetic field loop measured at 300 K and at 5 K for films on Si substrate. The curves measured from Ru-doped thin films: (2 × (100 × Fe_2O_3 + 100 × Ru) + 100 × Fe_2O_3) (a) and (25 × (10 × Fe_2O_3 + 10 × Ru)) (b) thin films deposited at 270 °C. The samples were measured on the Si substrate and the measured signal of the diamagnetic substrate is not removed (for illustration one hysteresis without Si substrate is depicted in the inset, (b)).

finite hysteresis width (coercive field H_c) of roughly 3 kOe (Fig. 9b) emerges at low temperatures in the Ru-doped film where the Ru content was 0.42 at%.

Superparamagnetic behavior is often expected in the case of small particles of magnetic materials, but it is also observable in a thin film containing nanocrystals.[19,20] The fact that the structures contain nanocrystals was confirmed by GIXRD (Fig. 3) and was visible from STEM images (Fig. 4). Similar size development of nanometer-sized magnetic ferrite particles powder (in ε-Fe_2O_3) was observed by Shin-ichi Ohkoshi *et al.*[18] Saturation magnetization in the present study was, however, observed already at room temperature. Zero field cooled (ZFC) and field cooled (FC) temperature dependence of susceptibility at applied field of 1000 Oe was measured in Ru-doped thin films with the recipe: 2 × (100 × Fe_2O_3 + 100 × Ru) + 100 × Fe_2O_3 and 25 × (10 × Fe_2O_3 + 10 × Ru). The blocking temperature estimated from the maxima in ZFC susceptibility for the Ru-doped film (Ru 0.42 at%) was 295 K, while in Ru-doped (Ru 0.98 at%) film much lower, 140 K (Fig. 10). Clearly, with increasing Ru content the superparamagnetic blocking

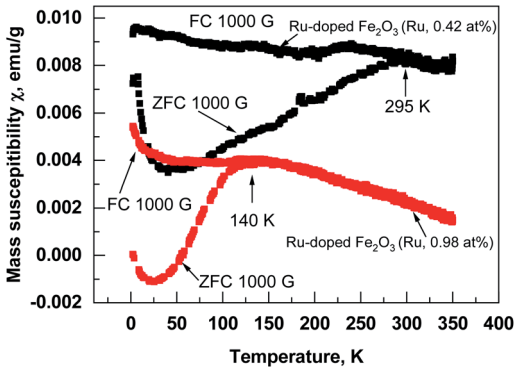

Fig. 10 Field cooled and zero-field cooled susceptibility curves measured from Ru-doped iron oxide structures (Ru content denoted by labels). Arrows indicate the estimated superparamagnetic blocking temperature of the nano-crystallites.

temperature decreased, which can be explained by the decrease of nano-crystals sizes of the film.

Conclusions

In conclusion, the atomic layer deposition of nano-crystallized Ru-doped iron oxide thin films containing hematite nanocrystals with size from 4 to 7.8 nm was realized in $FeCl_3$, $Ru(EtCp)_2$ and H_2O/O_2 process. The studies on three-dimensional, trenched structures confirmed that the Ru-doped Fe_2O_3 thin films could also be deposited to the inner regions of the 3D structures, which might be regarded as a pre-requisite to its possible medical applications. The structures in pure iron oxide films in the as-deposited state demonstrated ferromagnetic-like behavior at room temperature. The magnetization was nonlinear, with saturation and hysterese with well-defined coercive fields in most samples. The strongest coercive fields were determined in the samples where the ε-Fe_2O_3 phase dominated, and the highest H_c value was 18 kOe. Although the Ru-doped iron oxide thin films also demonstrated a behavior characteristic of superparamagnetic material, the finite hysteresis width was measured at low temperature. The strongest coercive field (3 kOe) was determined in Ru-doped samples at 5 K temperature, where the Ru content was 0.42 at% and crystallite size 4 nm.

Author contributions

Dr Aile Tamm planned the experiments and wrote the manuscript. Mr Aivar Tarre contributed to the thin film deposition and XRD analysis. Dr Jekaterina Kozlova analysed the material by scanning electron microscopy. Dr Mihkel Rähn analysed the material by transmission electron microscopy. Mr Tauno Kahro analysed the material by the micro Raman spectroscopy. Dr Taivo Jõgiaas contributed to material characterization by XRF. Mr Joosep Link analysed the material by VSM. Dr Raivo Stern supervised magnetic measurements and contributed to the writing of the manuscript.

Conflicts of interest

There are no conflicts to declare.

Acknowledgements

The study was partially supported by the European Regional Development Fund project "Emerging orders in quantum and nanomaterials" (TK134) and Estonian Research Agency project "Emerging Novel Phases in Strongly Frustrated Quantum Magnets" (PRG4).

References

1 A. V. Nikam, B. L. V. Prasad and A. A. Kulkarni, *CrystEngComm*, 2018, **20**, 5091.
2 R. M. Fratila, S. Rivera-Fernandez and J. M. de la Fuente, *Nanoscale*, 2015, **7**, 8233.
3 E. C. Abenojar, S. Wickramasinghe, J. Bas-Concepcion and A. C. S. Samia, *Prog. Nat. Sci.: Mater. Int.*, 2016, **26**, 440–448.
4 S. E. Gilliland III, E. C Shultz and M. D. Shultz, *Nanobiomedicine*, 2014, **1**, 9.
5 A. P. Romio, H. H. Rodrigues, A. Peres, A. D. C. Viegas, E. Kobitskaya, U. Ziener, K. Landfester, C. Sayer and P. H. H. Araújo, *J. Appl. Polym. Sci.*, 2013, **129**, 1426–1433.
6 R. W. Johnson, A. Hultqvist and S. F. Bent, *Mater. Today*, 2014, **17**, 236–246.
7 M. Leskelä and M. Ritala, *Angew. Chem., Int. Ed.*, 2003, **42**, 5548–5554.
8 K. V. Manukyan, Y.-S. Chen, S. Rouvimov, P. Li, X. Li, S. Dong, X. Liu, J. K. Furdyna, A. Orlov, G. H. Bernstein, W. Porod, S. Roslyakov and A. S. Mukasyan, *J. Phys. Chem. C*, 2014, **118**, 16264–16271.
9 X. Chen, J. Mao, C. Liu, C. Chen, H. Cao and L. Yu, *Chin. Chem. Lett.*, 2020, **31**, 3205–3208.
10 H. Seemen, K. Kukli, T. Jõgiaas, P. Ritslaid, J. Link, R. Stern, S. Duenas, H. Castan and A. Tamm, *J. Alloys Compd.*, 2020, **846**, 156099.
11 K. Kukli, J. Aarik, A. Aidla, I. Jõgi, T. Arroval, J. Lu, T. Sajavaara, M. Laitinen, A.-A. Kiisler, M. Ritala, M. Leskelä, J. Peck, J. Natwora, J. Geary, R. Spohn, S. Meiere and D. M. Thompson, *Thin Solid Films*, 2012, **520**, 2756–2763.
12 L. Machala, J. Tucek and R. Zboril, *Chem. Mater.*, 2011, **23**, 3255–3272.
13 P. Lotticia, C. Baratto, D. Bersani, G. Antonioli, A. Montenero and M. Guarneri, *Opt. Mater.*, 1998, **9**, 368–372.
14 A. Tanskanen, O. Mustonen and M. Karppinen, *APL Mater.*, 2017, **5**, 056104.
15 A. Tamm, K. Kalam, H. Seemen, J. Kozlova, K. Kukli, J. Aarik, J. Link, R. Stern, S. Duenas and H. Castan, *ACS Omega*, 2017, **2**, 8836–8842.
16 R. Kant, D. Kumar and V. Dutta, *RSC Adv.*, 2015, **5**, 52945.
17 L. Corbellini, J. Plathier, C. Lacroix, C. Harnagea, D. Menard and A. Pignolet, *J. Appl. Phys.*, 2016, **120**, 124101.
18 J. Jin, S. Ohkoshi and K. Hashimoto, *Adv. Mater.*, 2004, **16**, 48.
19 P.-C. Jianq, C.-H.-T. Chang, C.-Y. Hsieh, W.-B. Su and J.-S. Tsay, *Nanoscale*, 2020, **12**, 14096.
20 K. Kukli, M. Mikkor, A. Šutka, M. Kull, H. Seemen, J. Link, R. Stern and A. Tamm, *J. Magn. Magn. Mater.*, 2020, **498**, 166167.